Acoustic Proximity Ranging in the Presence of Secondary Echoes

Xi Li, *Student Member, IEEE*, Renbiao Wu, *Senior Member, IEEE*, Srihari Rasmi, Jian Li, *Senior Member, IEEE*, Louis N. Cattafesta, III, and Mark Sheplak

***Abstract*—Proximity ranging is very important in many applications. Ultrasonic sensors have proven to be very cost effective tools for this purpose. Most of the currently available time-of-flight based acoustic proximity ranging systems use the conventional matched filter based time delay estimation approaches to measure short distances between proximity objects. However, in the presence of strong and closely spaced secondary echoes, the aforementioned matched filter based algorithms tend to fail or suffer from severe performance degradations due to their poor resolutions. In this paper, a computationally efficient time delay estimation algorithm, referred to as multiecho parameter estimation for acoustic ranging systems, is described for the joint proximity range estimation and secondary echo mitigation. The effectiveness of the proposed algorithm is demonstrated by both numerical and experimental examples.**

***Index Terms*—Acoustic transducer, proximity ranging, secondary echoes, time delay estimation.**

I. Introduction

MEASURING the distance between a known base location and the surface of a proximal object is referred to as proximity ranging [1]. Proximity ranging is very important in a wide range of remote sensing applications, including level detection, robot manipulation, process control, nondestructive testing, and cavity thickness monitoring [1]–[4].

Various types of sensors based on different physical principles such as capacitive or inductive proximity sensors, laser displacement sensors, and ultrasonic sensors, can be used to perform proximity ranging [3]. Among these sensors, ultrasonic sensors have many important advantages over the others. First, they can operate in extreme environmental conditions, including in the presence of fog, dust, dirt, lighting or strong electromagnetic interference (EMI) radiation. Second, ultrasonic sensors can be used for accurate distance measurement by using the time-of-flight (TOF) principle. Moreover, due to the low speed of sound in air, the same distance resolution can be achieved by using much simpler electronic circuits for ultrasonic sensors than those for laser based sensors. Third, ultrasonic sensors can be fabricated at a low cost. Since generating ultrasound only requires the movement of a surface and can be effectively implemented by using electrostatic or piezoelectric devices, the fabrication cost for ultrasonic transducers is usually much lower than that of laser or microwave based sensors [22]. Indeed, ultrasonic sensors have proven to be very cost effective remote sensing tools for proximity ranging [5]–[7].

However, due to the presence of secondary echoes, using ultrasonic sensors for very close proximity ranging is very difficult. When ultrasonic sensors face a sound-hard reflective surface, the reflected sound wave can bounce back and forth several times between the sensors and the reflection surface before decaying to zero, which results in unwanted strong and overlapping secondary echoes in the received signal. The time delays for the secondary echoes are approximately integer multiples of the time delay of the first echo. The matched filter based methods cannot resolve two echoes with a time spacing less than the reciprocal of the signal bandwidth [8]. Hence, for most of the very short distance measurement scenarios, the matched filter based algorithms tend to fail or suffer from severe performance degradations due to their poor resolutions [9]. Most of the existing super-resolution time delay estimation approaches (see [10] and [11] and the references therein) are developed for general purposes. They do not exploit the *a priori* information of the integer multiple time delays and the nonnegative amplitude due to the acoustically hard reflections.

In this paper, we focus on acoustic proximity ranging in the presence of secondary echoes. A new time delay estimation method is proposed for the joint proximity ranging and secondary echo mitigation. We establish a flexible data model that takes into account the acoustically hard reflection as well as small random time delay variations of the secondary echoes around the integer multiples of the time delay of the first echo. The new time delay estimator is based on a nonlinear least squares (NLS) fitting criterion. However, it is difficult to directly optimize the highly nonlinear NLS cost function. We present a novel computationally efficient time delay estimation algorithm, referred to as multiecho parameter estimation for acoustic ranging systems (multi-PEARS), to optimize the NLS cost function.

The remainder of this paper is organized as follows. In Section II, we describe the data model and formulate the problem of interest. The multi-PEARS algorithm is presented in Section III. Numerical examples and experimental results

Manuscript received August 13, 2002; revised April 14, 2003. This work was supported in part by ONR, Advanced Technology Development for the Control of High-Speed Supercavitating Vehicles, under Grant N00014-00-1-0105.

X. Li and J. Li are with the Department of Electrical and Computer Engineering, University of Florida, Gainesville, FL 32611 USA (e-mail: li@dsp.ufl.edu).

R. Wu is with the Department of Electrical and Computer Engineering, University of Florida, Gainesville, FL 32611 USA. He is currently on leave from the Department of Communications Engineering, College of Air Traffic Management, Civil Aviation University of China, Tianjin, China.

S. Rasmi, L. N. Cattafesta III, and M. Sheplak are with the Department of Mechanical and Aerospace Engineering, University of Florida, Gainesville, FL 32611-6250 USA.

Digital Object Identifier 10.1109/TIM.2003.817907

Report Documentation Page

Form Approved
OMB No. 0704-0188

1. REPORT DATE	2. REPORT TYPE	3. DATES COVERED
APR 2003		**00-00-2003 to 00-00-2003**

4. TITLE AND SUBTITLE	5a. CONTRACT NUMBER
Acoustic Proximity Ranging in the Presence of Secondary Echoes	5b. GRANT NUMBER
	5c. PROGRAM ELEMENT NUMBER
6. AUTHOR(S)	5d. PROJECT NUMBER
	5e. TASK NUMBER
	5f. WORK UNIT NUMBER
7. PERFORMING ORGANIZATION NAME(S) AND ADDRESS(ES) **University of Florida,Department of Electrical and Computer Engineering,Gainesville,FL,32611**	8. PERFORMING ORGANIZATION REPORT NUMBER
9. SPONSORING/MONITORING AGENCY NAME(S) AND ADDRESS(ES)	10. SPONSOR/MONITOR'S ACRONYM(S)
	11. SPONSOR/MONITOR'S REPORT NUMBER(S)

12. DISTRIBUTION/AVAILABILITY STATEMENT
Approved for public release; distribution unlimited

13. SUPPLEMENTARY NOTES

14. ABSTRACT

15. SUBJECT TERMS

16. SECURITY CLASSIFICATION OF:			17. LIMITATION OF ABSTRACT	18. NUMBER OF PAGES	19a. NAME OF RESPONSIBLE PERSON
a. REPORT **unclassified**	b. ABSTRACT **unclassified**	c. THIS PAGE **unclassified**		**13**	

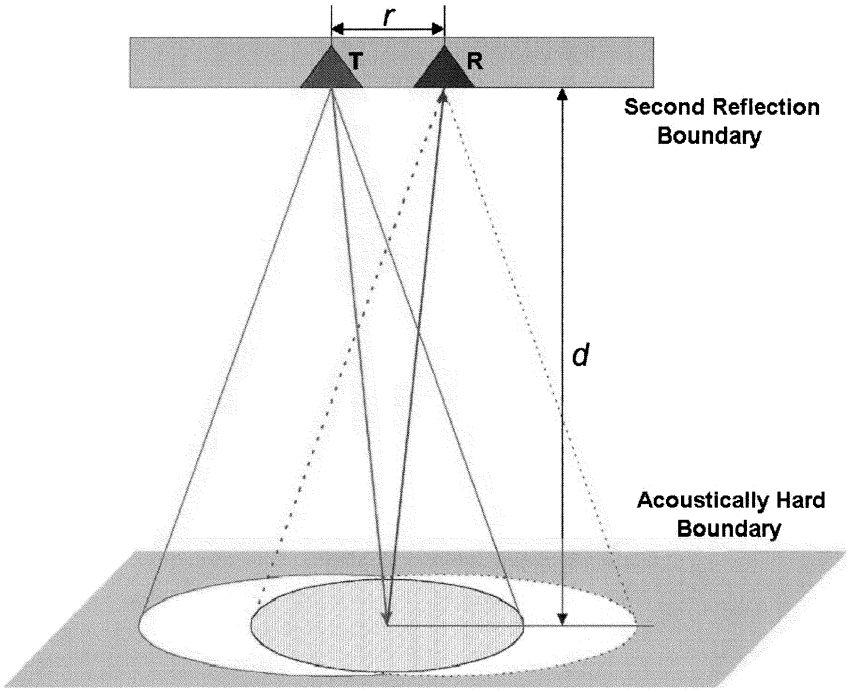

Fig. 1. Two-transducer acoustic proximity ranging system.

are given in Sections IV and V, respectively. Section VI concludes this paper. The derivations of the single-echo based PEARS algorithm (used in multi-PEARS) and the Cramér-Rao bounds (CRBs) corresponding to multi-PEARS are included in Appendices A and B, respectively.

II. Data Model and Problem Formulation

As shown in Fig. 1, a two-transducer ranging system is used to measure the distance between the transducers and an acoustically hard boundary. We assume that the propagation medium is homogeneous and nondispersive and the common region covered by both the transmitter and the receiver is a smooth planar surface. The transmitted signal is emitted from the transmitter toward the reflection boundary. The directly reflected signal received by the receiver is called the first echo. Since the distance between the sensors and the boundary is very short, the secondary reflections between the sensors and the ranging surface cannot be ignored. The time delays of the secondary echoes are approximately integer times of the time delay of the first echo. Hence the received signal can be modeled as

$$y(t) = \sum_{l=1}^{L} \alpha_l s(t - l\tau - \Delta_l) + e(t), \quad 0 \le t < T \tag{1}$$

where $s(t)$, $0 \le t < T$, represents the known (or measured) real-valued transmitted signal and T is the signal duration; $y(t)$ denotes the real-valued received signal; $\{\alpha_l\}_{l=1}^{L}$ denote the amplitudes of the received signal and α_1 is assumed to be nonnegative due to the acoustically hard reflection; τ denotes the time delay corresponding to the first echo, and the time delays for the secondary echoes are $l\tau + \Delta_l$, $l = 2, \ldots, L$, with $\Delta_1 \triangleq 0$ and $\{\Delta_l\}_{l=2}^{L}$ being small perturbations around the integer multiples of τ; $e(t)$ is the real-valued noise, which is modeled as a zero-mean Gaussian random process.

The received signal after sampling and A/D conversion has the form

$$y(nT_s) = \sum_{l=1}^{L} \alpha_l s(nT_s - l\tau - \Delta_l) + e(nT_s), \quad n = 0, 1, \ldots, N-1 \tag{2}$$

where T_s denotes the sampling period, which is equal to the reciprocal of the sampling frequency f_s.

Our problem of interest herein is to estimate τ from $\{y(nT_s)\}_{n=0}^{N-1}$ when $s(t)$, $0 \le t < T$, or more practically $\{s(nT_s)\}_{n=0}^{N-1}$ is known.

Instead of working on this problem in the time domain, the frequency domain is preferred. This is due to the following two reasons. First, for the time domain methods, we could either restrict τ to be multiples of T_s or resort to interpolation if only $\{s(nT_s)\}_{n=0}^{N-1}$ is known [11]. This inconvenience can be avoided by transforming the problem into the frequency domain, where τ can take on a continuum of values. Second, for the time domain data model in (2), $\{\alpha_l, \Delta_l\}_{l=2}^{L}$ for each secondary echo must be dealt with separately. However, by transforming (2) into the frequency domain and using the facts that $\{\Delta_l\}_{l=2}^{L}$ are small values, a more concise data model can be obtained.

Let $Y(m)$, $S(m)$, and $E(m)$, where $m = -N/2, -N/2 + 1, \ldots, N/2 - 1$, denote the discrete Fourier transforms (DFTs) of $y(nT_s)$, $s(nT_s)$, and $e(nT_s)$, respectively. Provided that the aliasing due to sampling is negligible, $Y(m)$ can be written as

$$Y(m) = \sum_{l=1}^{L} \alpha_l S(m) e^{-j\frac{2\pi}{NT_s}(l\tau + \Delta_l)m} + E(m). \tag{3}$$

Since both the transmitted signal $s(t)$ and the received signal $y(t)$ are real-valued, their Fourier transforms are conjugate

symmetric. Most of the currently available ultrasonic transducers are resonant devices that achieve high sensitivity at the frequency of less than 200 kHz and are narrowband systems [2]. Hence, the transmitted signal $s(t)$ is narrowband in general. In the negative frequency domain, i.e., for $m = -N/2, -N/2+1, \ldots, 0$, since $s(t)$ is narrowband, $S(m)$ mainly occupies a few frequency bins in the range $[m_0 - \Delta m, m_0 + \Delta m]$, where m_0 is the peak location of $|S(m)|$ and $2\Delta m \approx B_s N T_s$ with B_s being the signal bandwidth. Based on the above assumption and for very small $\{\Delta_l\}_{l=2}^{L}$, we have the following approximations for the signal term in (3):

$$\begin{aligned}\alpha_l S(m) e^{-j\frac{2\pi}{NT_s}(l\tau+\Delta_l)m} &= \alpha_l S(m) e^{-j\frac{2\pi}{NT_s}\Delta_l(m-m_0)} \\ &\quad \times e^{-j\frac{2\pi}{NT_s}\Delta_l m_0} e^{-j\frac{2\pi}{NT_s}l\tau m} \\ &\approx \alpha_l S(m) e^{-j\frac{2\pi}{NT_s}\Delta_l m_0} e^{-j\frac{2\pi}{NT_s}l\tau m} \\ &\triangleq \beta_l S(m) e^{-j\frac{2\pi}{NT_s}l\tau m} \end{aligned} \tag{4}$$

where $\beta_l \triangleq \alpha_l e^{-j((2\pi)/(NT_s))\Delta_l m_0}$, $l = 1, 2, \ldots, L$. Note that $\beta_1 = \alpha_1$ is nonnegative and $\{\beta_l\}_{l=2}^{L}$ are complex-valued. In the second step of deriving (4), we have assumed that $S(m) \approx 0$ for $m \notin [m_0 - \Delta m, m_0 + \Delta m]$ and $\{\Delta_l\}_{l=2}^{L}$ are so small that $((2\pi)/(NT_s))\Delta_l \Delta m \approx 0$ (i.e., $\pi \Delta_l B_s \approx 0$), and hence $e^{-j(2\pi)/(NT_s)\Delta_l(m-m_0)} \approx 1$ for $m \in [m_0 - \Delta m, m_0 + \Delta m]$. Therefore, the small time delay variations of the secondary echoes have been transformed to the phases of their complex amplitudes.

Based on (3) and (4), and by exploiting the conjugate symmetry property of $Y(m)$, $S(m)$, and $E(m)$, the unknown parameters can be obtained by minimizing the following NLS criterion:

$$\mathcal{L}_1(\{\boldsymbol{\beta}, \tau\}) = \sum_{m=-\frac{N}{2}}^{0} P^2(m) \left| Y(m) - S(m) \sum_{l=1}^{L} \beta_l e^{-j\frac{2\pi l\tau}{NT_s}m} \right|^2 \tag{5}$$

where $\boldsymbol{\beta} = [\beta_1 \ \beta_2 \ \cdots \ \beta_L]^T$ with $(\cdot)^T$ denoting the transpose, $\{P(m) = 1\}_{m=-N/2+1}^{-1}$, and $P(-N/2) = P(0) = (1/\sqrt{2})$.

Define

$$\begin{aligned}\mathbf{x} = \Bigg[P\left(-\frac{N}{2}\right) Y\left(-\frac{N}{2}\right) \quad P\left(-\frac{N}{2}+1\right) Y\left(-\frac{N}{2}+1\right) \\ \cdots \quad P(0)Y(0) \Bigg]^T \end{aligned} \tag{6}$$

where $K = N/2 + 1$ is the dimension of the vector $\mathbf{x}$. Let $\mathbf{W}$ be a $K \times K$ diagonal matrix

$$\begin{aligned}\mathbf{W} = \operatorname{diag}\Bigg\{ &P\left(-\frac{N}{2}\right) S\left(-\frac{N}{2}\right), \\ &P\left(-\frac{N}{2}+1\right) S\left(-\frac{N}{2}+1\right), \cdots, P(0)S(0) \Bigg\}. \end{aligned} \tag{7}$$

Let

$$\begin{aligned}\mathbf{b}(l\tau) &= \left[e^{-j\frac{2\pi l\tau}{NT_s}(-\frac{N}{2})} \quad e^{-j\frac{2\pi l\tau}{NT_s}(-\frac{N}{2}+1)} \quad \cdots \quad 1 \right]^T \\ &= [e^{-j2\pi f_0 l\tau} \quad e^{-j2\pi f_1 l\tau} \quad \cdots \quad e^{-j2\pi f_{K-1} l\tau}]^T \end{aligned} \tag{8}$$

where

$$f_k = -\frac{1}{2T_s} + \frac{k}{NT_s}, \quad k = 0, 1, \ldots, K-1. \tag{9}$$

Define

$$\mathbf{B}(\tau) = [\mathbf{b}(\tau) \quad \mathbf{b}(2\tau) \quad \cdots \quad \mathbf{b}(L\tau)] \tag{10}$$

and

$$\mathbf{D}(\tau) = \mathbf{W}\mathbf{B}(\tau). \tag{11}$$

Then (5) can be expressed as

$$\mathcal{L}_1(\{\boldsymbol{\beta}, \tau\}) = \|\mathbf{x} - \mathbf{D}(\tau)\boldsymbol{\beta}\|^2 \tag{12}$$

where $\|\cdot\|$ denotes the Euclidean norm. For the white noise case, the above NLS approach is the same as the maximum likelihood (ML) method. When the noise is colored, the NLS approach can still give very accurate parameter estimates [12].

We remark that the time delay estimation problem considered herein is similar to the well-known harmonic sinusoidal parameter estimation problem [13]–[15]. However, the sinusoidal signals in our problem are weighted by the known signal spectrum and the amplitude for the first echo is nonnegative. Since most of the existing harmonic retrieval methods are designed for signals with complex-valued amplitudes and flat band-limited spectra, they are not directly applicable to our problem of interest.

Note that minimizing (12) is a highly nonlinear optimization problem. We present below an efficient optimization method, referred to as the multi-PEARS algorithm, to minimize (12) by taking into account both nonnegative β_1 and the weighted harmonic structure of the data model.

III. Multi-PEARS Algorithm

The multi-PEARS algorithm optimizes the NLS cost function iteratively. First, we assume all of the amplitudes $\{\beta_l\}_{l=1}^{L}$ are complex-valued and obtain an initial estimate by minimizing (12) via a fast Fourier transform (FFT)-based method. Next, based on the initial estimates, we subtract out the components of the secondary echoes and keep only the component of the first echo. Then, the single-echo based PEARS algorithm [16] is used to refine the initial time delay estimate. The refining step is iterated several times.

A. Initialization Stage

Assume that $\{\beta_l\}_{l=1}^{L}$ are complex-valued, it can be shown that the unknown parameters minimizing (12) can be determined by [17]

$$\hat{\tau}_0 = \arg\max_{\tau} c_0(\tau) \tag{13}$$

where

$$c_0(\tau) \triangleq \mathbf{x}^H \mathbf{D}(\tau) \left[\mathbf{D}^H(\tau)\mathbf{D}(\tau)\right]^{-1} \mathbf{D}^H(\tau)\mathbf{x} \tag{14}$$

and

$$\hat{\boldsymbol{\beta}}_0 = \left[\mathbf{D}^H(\tau)\mathbf{D}(\tau)\right]^{-1} \mathbf{D}^H(\tau)\mathbf{x}|_{\tau=\hat{\tau}_0} \tag{15}$$

with $(\cdot)^H$ denoting the conjugate transpose. According to the parsimony principle [18], if β_1 is indeed nonnegative, the estimate obtained by maximizing $c_0(\tau)$ should be less accurate than that obtained by minimizing the true cost function of (12). Note that (13) is a one-dimensional search problem and $c_0(\tau)$

usually has many local maxima. Hence, maximizing $c_0(\tau)$ requires the search over a very fine grid. By taking advantage of the harmonic structure of the data model, we use zero-padding FFT to perform such a search computationally efficiently.

Note that $\mathbf{D}^H(\tau)\mathbf{D}(\tau)$ in (14) can be expressed as

$$\mathbf{D}^H(\tau)\mathbf{D}(\tau) = \begin{bmatrix} d_0 & d_1 & \dots & d_{L-1} \\ d_1^* & \ddots & \ddots & \vdots \\ \vdots & \ddots & \ddots & d_1 \\ d_{L-1}^* & \dots & d_1^* & d_0 \end{bmatrix}_{L\times L} \tag{16}$$

where $(\cdot)^*$ denotes the complex conjugate and

$$\begin{aligned} d_l &= \sum_{k=0}^{K-1} |W(k)|^2 e^{-j2\pi f_k l\tau} \\ &= e^{j\frac{N\omega}{2}} \sum_{k=0}^{\frac{N}{2}} |W(k)|^2 e^{-j\omega k}\Big|_{\omega=\frac{2\pi l\tau}{NT_s}}, \\ & l = 0,1,\dots,L-1 \end{aligned} \tag{17}$$

with $W(k)$ denoting the kth diagonal element of the diagonal matrix $\mathbf{W}$ in (7), and $\mathbf{x}^H\mathbf{D}(\tau)$ can be expressed as

$$\mathbf{x}^H\mathbf{D}(\tau) = [a_1 \quad a_2 \quad \cdots \quad a_L] \tag{18}$$

where

$$\begin{aligned} a_l &= \sum_{k=0}^{K-1} [x^*(k)W(k)] e^{-j2\pi f_k l\tau} \\ &= e^{j\frac{N\omega}{2}} \sum_{k=0}^{\frac{N}{2}} [x^*(k)W(k)] e^{-j\omega k}\Big|_{\omega=\frac{2\pi l\tau}{NT_s}}, \\ & l = 1,2,\dots,L \end{aligned} \tag{19}$$

with $x(k)$ denoting the kth element of $\mathbf{x}$ in (6).

It can be seen from (17) and (19) that $\{d_l\}_{l=0}^{L-1}$ and $\{a_l\}_{l=1}^{L}$ can be obtained as follows. First, the discrete time Fourier transform (DTFT), which can be efficiently implemented by using zero-padding FFT, is applied to the sequences $\{|W(k)|^2\}_{k=0}^{N/2}$ and $\{x^*(k)W(k)\}_{k=0}^{N/2}$, respectively. Next, the linear phase term $e^{j(N\omega/2)}$ is multiplied to the outputs of DTFT, and finally, the sampling is performed at the frequency points $\omega = (2\pi l\tau)/(NT_s)$.

Define the following two vectors which are obtained by multiplying the phase term $e^{j(N\omega)/(2)}$ to the FFTs of $\{|W(k)|^2\}_{k=0}^{N/2}$ and $\{x^*(k)W(k)\}_{k=0}^{N/2}$, respectively, as

$$\mathbf{q} = \begin{bmatrix} q(0) & q(1) & \cdots & q(\tilde{N}-1) \end{bmatrix}^T \tag{20}$$

and

$$\mathbf{r} = \begin{bmatrix} r(0) & r(1) & \cdots & r(\tilde{N}-1) \end{bmatrix}^T \tag{21}$$

where $\tilde{N}$ denotes the data length after zero-padding. For $\tilde{N}$ sufficient large and for any given τ and l, the corresponding d_l and a_l can be approximately obtained by picking the elements of $\mathbf{q}$ and $\mathbf{r}$ at the index $\lfloor(\tilde{N}l\tau)/(NT_s)\rfloor$, where $\lfloor\cdot\rfloor$ denotes rounding to the nearest integer. Once $\{d_l\}_{l=0}^{L-1}$ and $\{a_l\}_{l=1}^{L}$ are in hand, $\mathbf{D}^H(\tau)\mathbf{D}(\tau)$ and $\mathbf{x}^H\mathbf{D}(\tau)$ can be constructed and substituted into (14) to obtain the cost function $c_0(\tau)$ at the τ. The calculation steps for the initial estimation can be summarized as follows.

Step 1) Zero-pad $\{|W(k)|^2\}_{k=0}^{N/2}$ and $\{x^*(k)W(k)\}_{k=0}^{N/2}$ to length of $\tilde{N}$ and perform $\tilde{N}$-point FFTs. Compensate out the linear phase term $e^{j(N\omega)/(2)}$ for the FFTs and obtain the data vectors $\mathbf{q}$ and $\mathbf{r}$, respectively.

Step 2) For a given τ, obtain d_l and a_l as

$$d_l = q\left(\left\lfloor\frac{(\tilde{N}\tau l)}{(NT_s)}\right\rfloor\right), \quad l = 0,1,\cdots,L-1 \tag{22}$$

and

$$a_l = r\left(\left\lfloor\frac{(\tilde{N}\tau l)}{(NT_s)}\right\rfloor\right), \quad l = 1,2,\cdots,L. \tag{23}$$

Step 3) Construct $\mathbf{D}^H(\tau)\mathbf{D}(\tau)$ and $\mathbf{x}^H\mathbf{D}(\tau)$ by using $\{d_l\}_{l=0}^{L-1}$ and $\{a_l\}_{l=1}^{L}$ obtained in Step (2). Compute $c_0(\tau)$ for the given τ based on (14).

Step 4) According to the maximum peak location of the computed $c_0(\tau)$ in Step (3), obtain the initial estimate $\hat{\tau}_0$ of τ. Once $\hat{\tau}_0$ is obtained, $\hat{\boldsymbol{\beta}}_0$ can be readily calculated by using (15).

In practical applications, we have used $\tilde{N} = 4N$, which is sufficiently accurate for the initial estimation in our examples. Note also that in the above search method, we need to compute the FFTs of $\{|W(k)|^2\}_{k=0}^{N/2}$ and $\{x^*(k)W(k)\}_{k=0}^{N/2}$ only once. Thereafter, the look-up table method is used to find $\{d_l\}_{l=0}^{L-1}$ and $\{a_l\}_{l=1}^{L}$ for a given τ. Thus, this method is computationally more efficient than the brute force search method, and can be easily implemented by currently available dedicated FFT chips.

B. Refining Stage

Assume $\{\hat{\beta}_l\}_{l=2}^{L}$ and $\hat{\tau}$ are given, we subtract out the secondary echoes to obtain

$$\mathbf{x}_1 = \mathbf{x} - \sum_{l=2}^{L} \hat{\beta}_l \mathbf{W}\mathbf{b}(l\hat{\tau}). \tag{24}$$

Then (12) becomes

$$\mathcal{L}_2(\{\beta_1,\tau\}) = \|\mathbf{x}_1 - \beta_1\mathbf{W}\mathbf{b}(\tau)\|^2 \tag{25}$$

where β_1 is assumed to be nonnegative due to the acoustically hard reflection. We have developed an efficient optimization algorithm, referred to as PEARS, to solve the time delay estimation problem for this single echo case [16]. To make this paper self-contained, the derivation of the PEARS algorithm is given in Appendix A. Note that PEARS is a two-stage algorithm which first obtains an initial estimate based on a smooth cost function, and then refines the initial estimate based on the true cost function. Herein, since we have already obtained the initial estimate of τ, we only need to use the second stage of PEARS to refine it. Note that iteration can improve the accuracy of $\hat{\tau}$. The refined estimate $\hat{\tau}$ can be used to redetermine $\hat{\boldsymbol{\beta}}$ via (15). Then the refined $\hat{\tau}$ and $\hat{\boldsymbol{\beta}}$ are used to redetermine $\mathbf{x}_1$ by using (24).

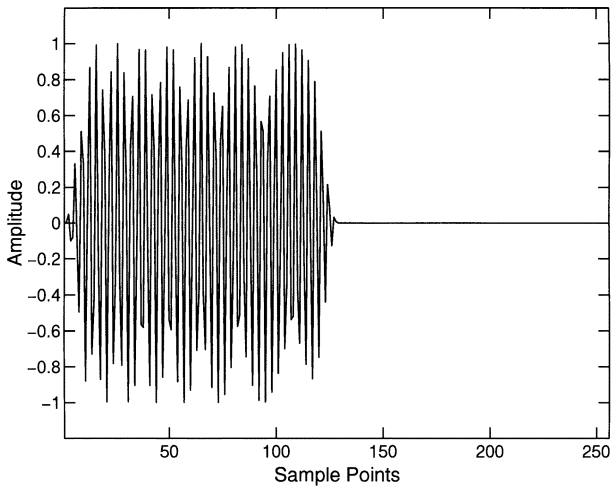

(a)

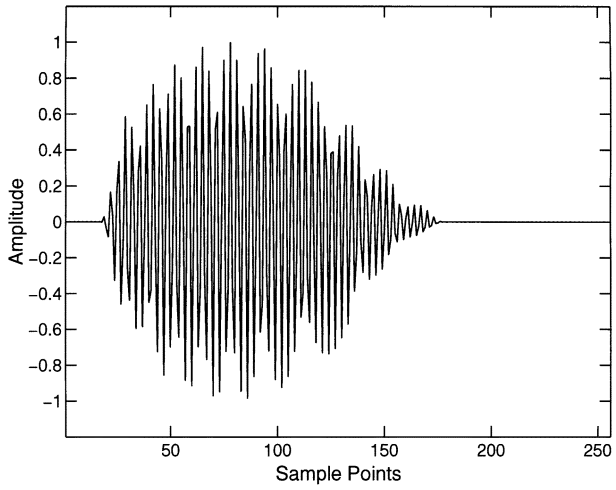

(b)

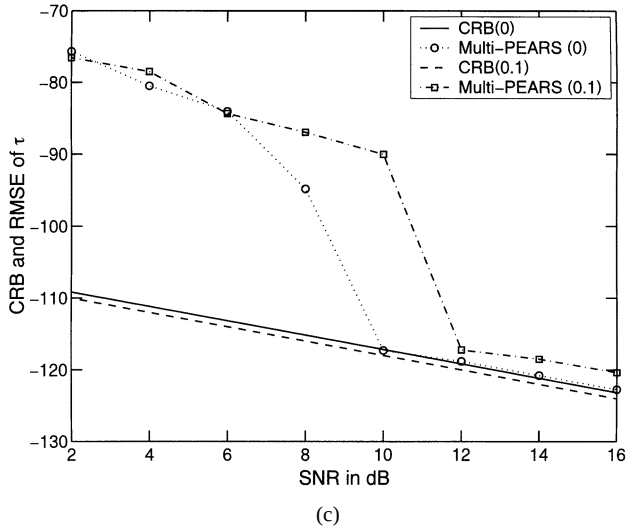

(c)

Fig. 2. Numerical results. (a) Transmitted signal. (b) Received signal in the absence of noise. (c) Comparison of the RMSEs of the estimates and the corresponding CRBs for τ. Two different cases for the time delay variations of the secondary echoes are illustrated: 1) $\Delta_2 = \Delta_3 = 0$. The RMSEs and the corresponding CRB are denoted as the circles and the solid line, respectively. 2) $\Delta_2 = \Delta_3 = 0.1\ T_e$. The RMSEs and the corresponding CRB are denoted as the squares and the dashed line, respectively.

Based on the updated $\mathbf{x}_1$, a more accurate estimate $\hat{\tau}$ of τ can be obtained by using PEARS. With the above simple preparations, we now present the steps of the multi-PEARS algorithm.

Step 1) Obtain the initial estimates $\hat{\tau}_0$ and $\hat{\boldsymbol{\beta}}_0$ by using the FFT-based method proposed in Section III-A. Let $\hat{\tau} = \hat{\tau}_0$ and $\hat{\boldsymbol{\beta}} = \hat{\boldsymbol{\beta}}_0$.

Step 2) Obtain $\mathbf{x}_1$ by using (24).

Step 3) Obtain the refined $\hat{\tau}$ by using the second stage of PEARS as follows:

Substep 3.1: Obtain the measurement for each frequency point as $\breve{x}_k = W^*(k)x_1(k)$, $k = 0, 1, \ldots, K-1$, where $x_1(k)$ denotes the kth element of $\mathbf{x}_1$.

Substep 3.2: Obtain the phase for each measurement by $\breve{\theta}_k = -\arg(\breve{x}_k)$, $k = 0, 1, \ldots, K-1$, where $\arg(x)$ denotes the phase of x.

Substep 3.3: Obtain the integers $z_k = \lfloor((2\pi f_k\hat{\tau} - \breve{\theta}_k)/(2\pi))\rfloor, k = 0, 1, \ldots, K-1$, where f_k is defined in (9) and $\lfloor\cdot\rfloor$ denotes rounding to the nearest integer.

Substep 3.4: Obtain the refined $\hat{\tau}$ via $\hat{\tau} = (\sum_{k=0}^{K-1} |\breve{x}_k| f_k(\breve{\theta}_k + 2\pi z_k))/(\sum_{k=0}^{K-1} 2\pi|\breve{x}_k| f_k^2)$.

Step 4: Determine refined $\hat{\boldsymbol{\beta}}$ via (15) by using the refined $\hat{\tau}$.

Step 5: Iterate **Steps 2** through **4** and calculate the residue after each iteration as $\|\mathbf{x} - \mathbf{D}(\hat{\tau})\hat{\boldsymbol{\beta}}\|^2$. If the relative change of the residues between two consecutive iterations is less than a small value ϵ, the algorithm stops (in our examples, we have used $\epsilon = 10^{-4}$ to test the convergence of the algorithm).

Before we proceed, let us remark on the following two facts. First, multi-PEARS converges very fast due to the good initial estimates. In practice, we note that the algorithm usually converges within three or four iterations. Second, the number of the echoes L is determined by the practical measurement environment. Whenever L is unknown, it can be estimated from $\mathbf{x}$ by using, for instance, the generalized Akaike information criterion [12].

IV. Numerical Examples

To demonstrate the estimation accuracy of the proposed multi-PEARS algorithm, we present a numerical example below based on a windowed chirp signal. The transmitted signal is defined as

$$s(t) = w(t)\cos\left[2\pi f_c t + \gamma\left(t - \frac{T_0}{2}\right)^2\right], \quad 0 \le t < T \tag{26}$$

where f_c denotes the carrier frequency, γ represents the chirp rate, and

$$w(t) = \begin{cases} 0.5 - 0.5\cos\left(\frac{\pi t}{T_w}\right), & 0 < t < T_w, \\ 1, & T_w \le t \le T_0 - T_w, \\ 0.5 - 0.5\cos\left[\frac{\pi(t-T_0)}{T_w}\right], & T_0 - T_w < t \le T_0 \end{cases} \tag{27}$$

with $T_w = T_0/10$. In the following simulations, we use $N = 256$, $\gamma = 2.5\pi \times 10^4$, the signal bandwidth $B_s = \gamma T_0/\pi$, the carrier frequency $f_c = 10B_s$, and the sampling frequency

$f_s = 32B_s$. T_0 is chosen in such a way that $T_0 = \sqrt{N\pi/64\gamma} = 12.6$ ms. Thus $T_s = 98.821$ μs, $B_s = 0.316$ kHz, $f_c = 3.16$ kHz, $f_s = 10.12$ kHz, and $T = 25.3$ ms. Define the reciprocal of the signal bandwidth as $T_e \triangleq 1/B_s = 3.2$ ms. For the received signal, $\tau = 16.2\ T_s = 0.506\ T_e$, $\alpha_1 = 0.5$, $\alpha_2 = 0.3$, $\alpha_3 = 0.1$. Note that the time delay between each echo is only about one half of T_e. Thus, the first echo and secondary echoes cannot to be resolved by using the matched filter based methods in this case. The SNR (signal-to-noise ratio) is defined as $10\log_{10}(\alpha_1^2 E_s/(N\sigma^2))$, where E_s is the energy of the signal $s(nT_s)$. The root-mean-squared errors (RMSEs) are obtained through 300 Monte Carlo trials.

The waveforms of the transmitted signal and the noise free received signal are compared in Fig. 2(a) and (b). In Fig. 2(c), the RMSEs of the estimates of τ are compared with the corresponding CRBs, which are the best performance bounds for any unbiased estimators (the CRBs are derived in Appendix B). Two different cases for the time delay variations of the secondary echoes are illustrated: 1) $\Delta_2 = \Delta_3 = 0$, and 2) $\Delta_2 = \Delta_3 = 0.1\ T_e$. In case (1), the RMSEs of the estimates and the corresponding CRB are denoted as the circles and the solid line, respectively. In case (2), the RMSEs of the estimates and the corresponding CRB are denoted as the squares and the dashed line, respectively. It can be seen that when there are no time delay variations for the secondary echoes (i.e., $\Delta_2 = \Delta_3 = 0$), the RMSEs of the estimates can achieve the corresponding CRB. Note also the threshold effects where the RMSEs of the estimates deviate from the CRB when the SNR is less than 10 dB. When there exist the time delay variations for the secondary echoes, the estimates are biased and the RMSEs of the estimates cannot achieve the corresponding CRB. However, if the time delay variations are very small compared with the reciprocal of the signal bandwidth, the RMSEs of the estimates can still approach the corresponding CRB, and thus our method can achieve a high estimation accuracy in these cases as well. In the low SNR range, the RMSEs of the estimates deviate from the true CRB because the algorithm can no longer resolve the true peak of the highly oscillatory cross correlation function between the received signal and the reference signal. However, in this case, a reliable estimate can still be obtained based on the peak of the envelope of the cross correlation function [19], which corresponds to obtaining the estimate by using the first stage of our algorithm.

Fig. 3(a)–(c) illustrates the RMSEs of the estimates compared with the CRBs as the function of time delay by fixing the SNR. The time delays are normalized to T_e and we assume $\Delta_2 = \Delta_3 = 0$. It can be seen that as the time delay decreases, the corresponding CRB increases. This is as expected because the smaller the time delay, the more the echoes are overlapped, and hence the worse the estimation accuracy. Noted also the threshold effects in Fig. 3(a) and (b), where the RMSEs of estimates deviate from the CRB when the time delay is less than a certain value. In order to still achieve the corresponding CRB in the smaller time delay region, the higher SNR is required.

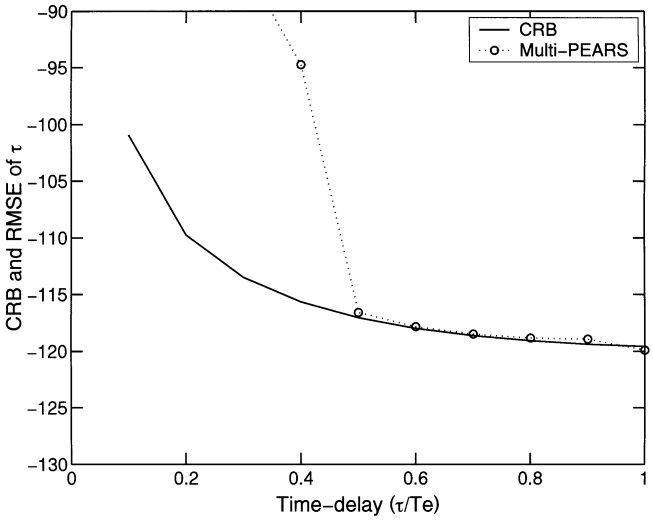

(a)

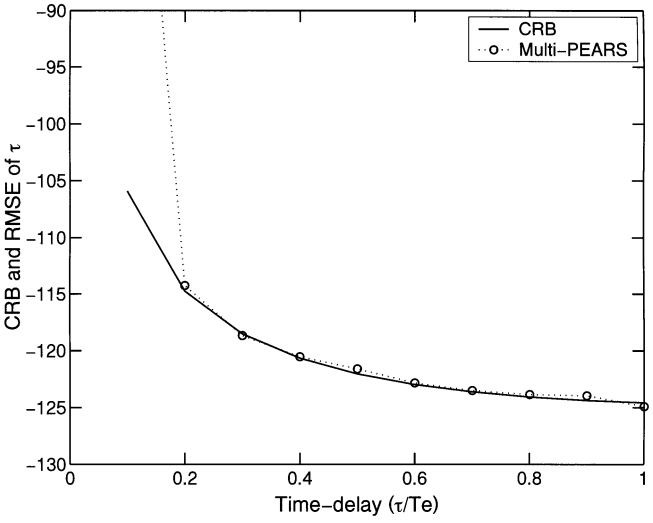

(b)

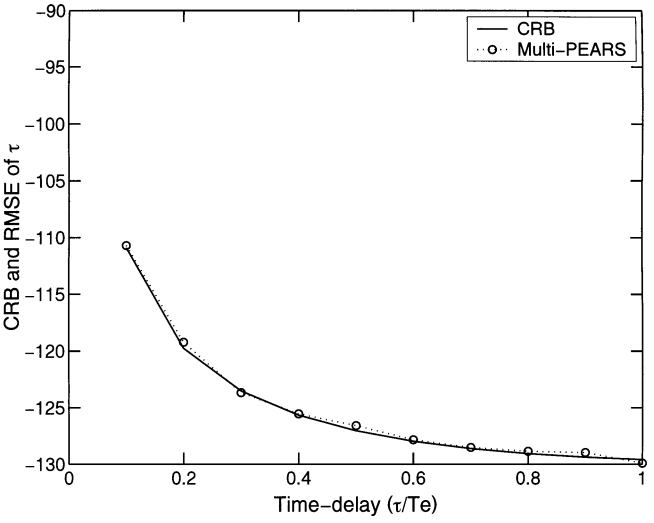

(c)

Fig. 3. RMSEs and CRBs versus the normalized time delay at different SNRs. The time delays are normalized to T_e, which is the reciprocal of the signal bandwidth. (a) $\mathrm{SNR} = 10$ dB, (b) $\mathrm{SNR} = 15$ dB, and (c) $\mathrm{SNR} = 20$ dB.

V. Experimental Results

Experiments have been conducted by using the commercially available Panasonic ceramic transducers (EFRRSB40K5 and

TABLE I
PARAMETERS OF THE PANASONIC ULTRASONIC CERAMIC TRANSDUCERS

Part No.	EFRRSB40K5	EFRTSB40K5
Application	Receiver	Transmitter
Resonant Frequency (kHz)	40	40
Bandwidth (kHz)	4	4
Sensitivity (dB)*	-50	---
Sound Pressure Level (dB)**	---	105
Maximum Input Voltage (Vrms)	---	20

* 0 dB=1 V/Pa ** 0 dB=2×10^{-5} Pa

EFRTSB40K5). Table I lists the parameters of the transducers used in our experiments [20]. The block diagram of the experimental setup and the photograph for the acoustic ranging system are shown in Fig. 4(a) and (b), respectively. The geometric centers of the two transducers are 17-mm apart and they are mounted above an aluminum plate with a smooth surface, which is used to simulate the planar acoustically hard boundary. The acoustic transducers are fixed on a three–dimensional (3-D) traverse controlled by a personal computer (PC), which is used to adjust the position of the transducers related to the boundary with an accuracy of 0.4 μm. The excitation signal for the transmitter is a pulse burst generated by an arbitrary waveform generator. The pulse repetition frequency is 192 Hz and the pulse width is 0.15 ms. Each pulse has been modulated by a carrier frequency of 40 kHz, which is the resonant frequency of the transducer. A 16-bit ADC is used to sample ($f_s = 196\,608$ Hz) the excitation signal for the transmitter and the received signal from the receiver. The recorded data are transferred to a host PC and the multi-PEARS algorithm is applied to the recorded data to determine the distance estimates. The sound speed is obtained by [21]

$$c = \sqrt{\gamma R T_r} \tag{28}$$

where $\gamma = 1.4$ is the ratio of specific heats, $R = 287\,\mathrm{J/(kg \cdot K)}$ is the gas constant, and $T_r = (273.16 + 21)\,\mathrm{K}$ in our experiments. Thus we have $c = 344\ \mathrm{m/s}$. In our experiments, since the transmitter and the receiver are closely placed, there exists a small amount of crosstalk. Note that the crosstalk is unchanged and independent of the reflected signal, and hence it can be recorded and stored in the system in advance and subtracted out from each received signal thereafter. All the received signals below are illustrated after the crosstalk subtraction.

Fig. 5 shows the recorded signals in the experiments. Fig. 5(a) is the transmitted signal, which is obtained when the transmitter and the receiver are face to face. The distance between the transducers has been measured precisely. Thus this waveform is taken as the known transmitted waveform. Fig. 5(b) shows the discrete Fourier transform (magnitude) of the signal in Fig. 5(a). It can be seen that the transmitted signal is narrowband with the bandwidth about 4 kHz. Thus, the nominal minimum distance required to resolve the first and secondary echoes by the matched filter method is about 43 mm.

We then increase the distance between the transducers to the boundary starting at 29 mm. The entire measurement range is exactly 10 mm and is covered in 21 discrete levels. The distance

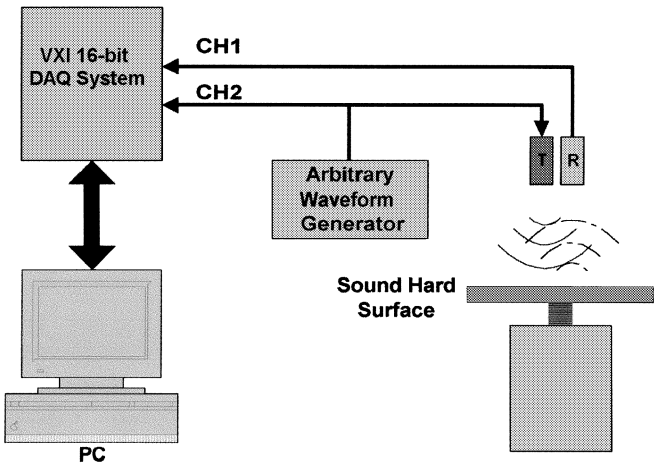

(a)

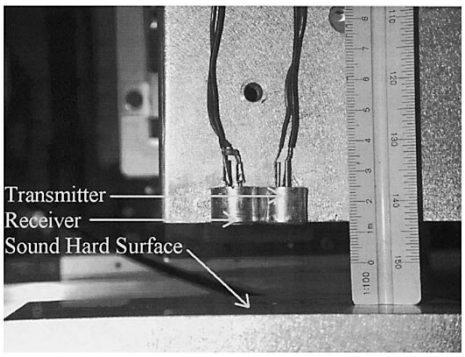

(b)

Fig. 4. Experimental setup for the acoustic ranging system. (a) Block diagram of the experimental setup. (b) Photograph of the setup for the sensors and the boundary.

difference between two consecutive levels is 0.5 mm. Fig.5(c) to (f) show the measured waveforms recorded at the levels 3, 5, 15, and 19, respectively. As we can see that due to the presence of the secondary echoes, the shapes of the received signals at different levels are quite different. For the noise in this experiment, the electronic noise dominates and the SNR is about 20 dB based on the definition in Section IV. In the practical environment, the noise level can be much higher due to the presence of the environmental noise. However, for a steady and controllable environmental noise, one can obtain it by using another receiver independently driven, and remove it from the real received signals thereafter.

Fig. 6 shows an example where the multi-PEARS algorithm is applied to the recorded signal at level 19. We use generalized Akaike information criterion to determine the number of the echoes and obtain $L = 4$ for this example. It can be seen from this figure that multi-PEARS can correctly resolve the first and secondary echoes even though they are heavily overlapped. Note also that the reconstructed signal matches the original signal very well. The relative error between these two signals is only 0.7%.

Fig. 7 shows the measurement results for the entire range with the different choices for L (the number of echoes). If the secondary echoes are not taken into account and $L = 1$ is used, an accurate $\hat{\tau}$ cannot be obtained. By using $L = 2$,

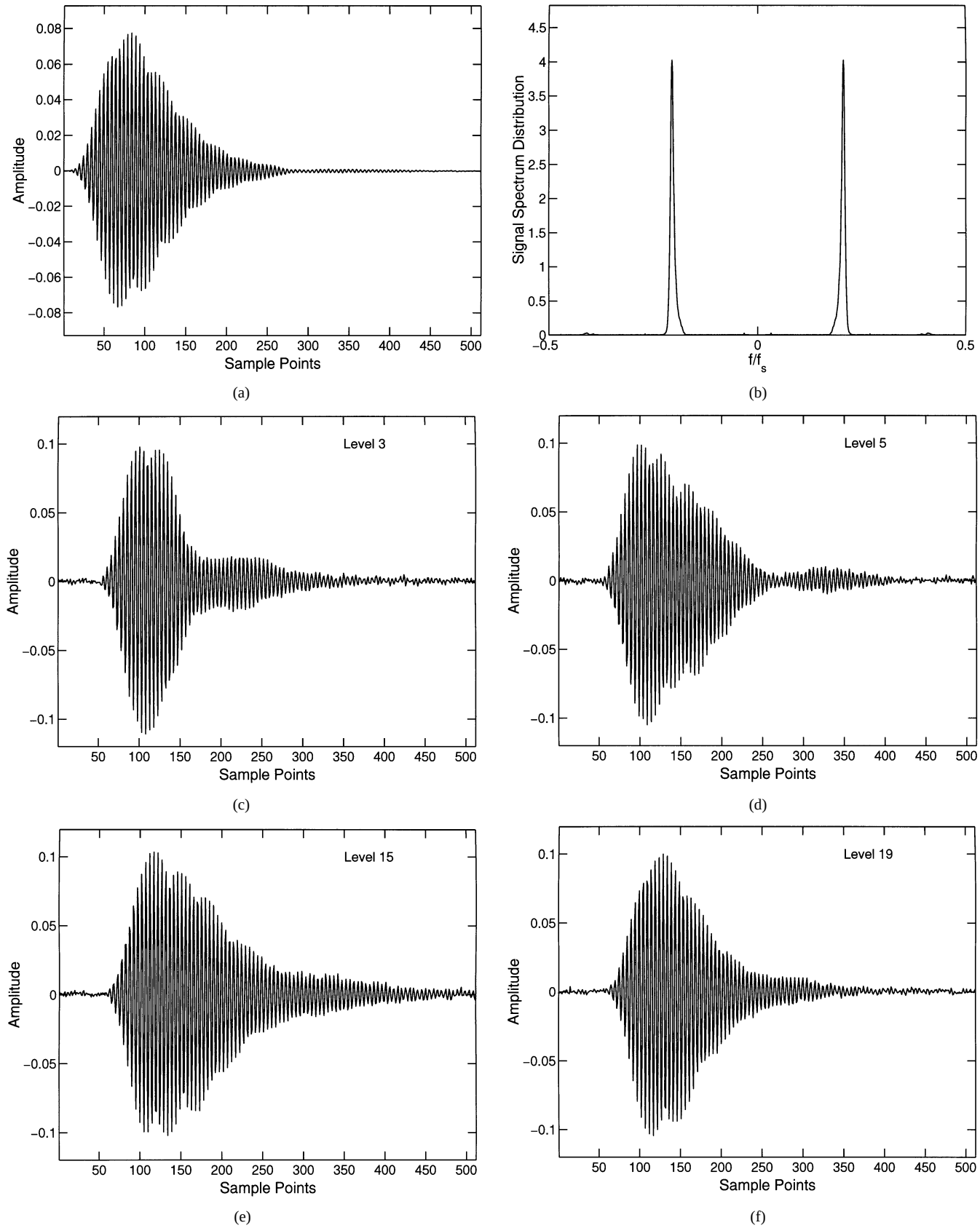

Fig. 5. Recored waveforms in the real experiment. (a) Transmitted waveform. (b) Discrete Fourier transform of signal in (a). (c) Received signal at level 3. (d) Received signal at level 5. (e) Received signal at level 15. (f) Received signal at level 19.

the measurement results are improved. But there are still four levels where the measurements are quite different from the true distances. (The results for $L = 3$ are similar to those of $L = 2$.) By using $L = 4$, very good results are obtained for

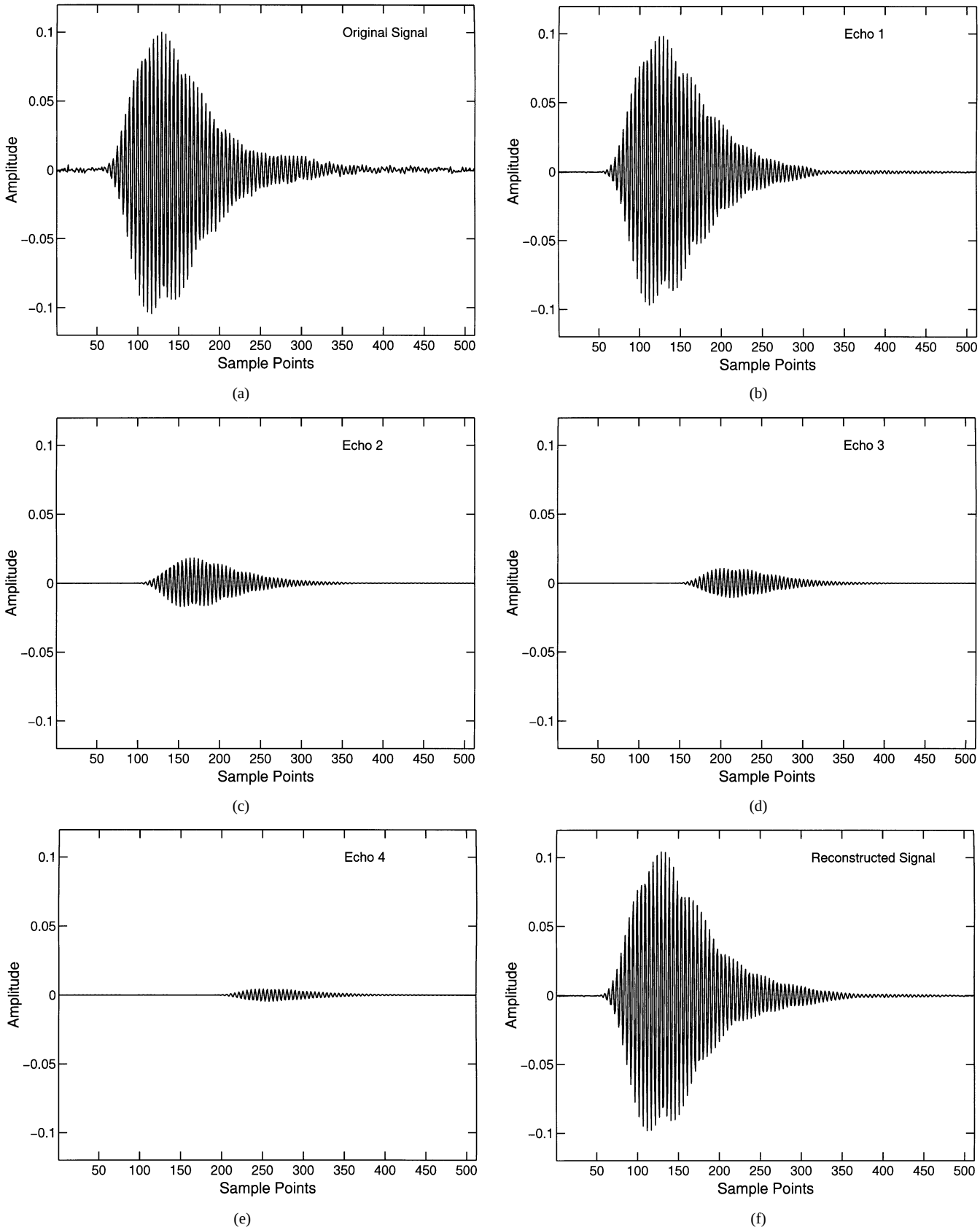

Fig. 6. Application of multi-PEARS to a recorded signal at level 19. (a) The original signal. (b)–(e) The reconstructed signals by using multi-PEARS estimates for the echoes 1 to 4, respectively. (d) The reconstructed signal by superposition of the signals in (b)–(e).

all distances. The zoomed-in view of the measurement errors are shown in Fig. 7(b). Note that the maximum measurement error is about 0.02 mm for $L = 4$. The ratio between this error and the entire measurement range is 2×10^{-3}.

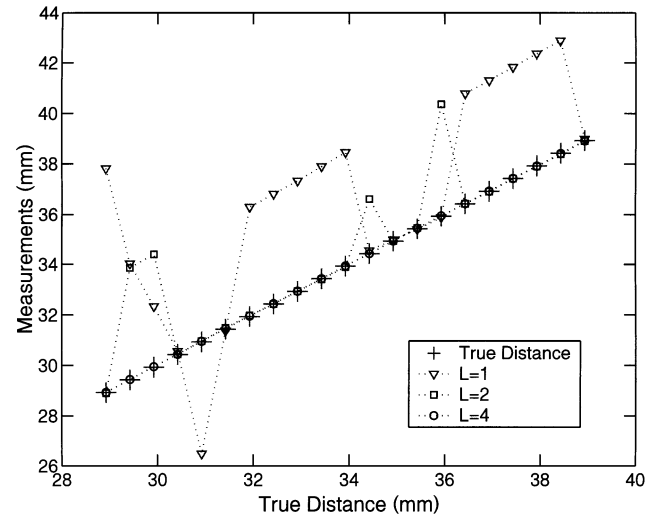

(a)

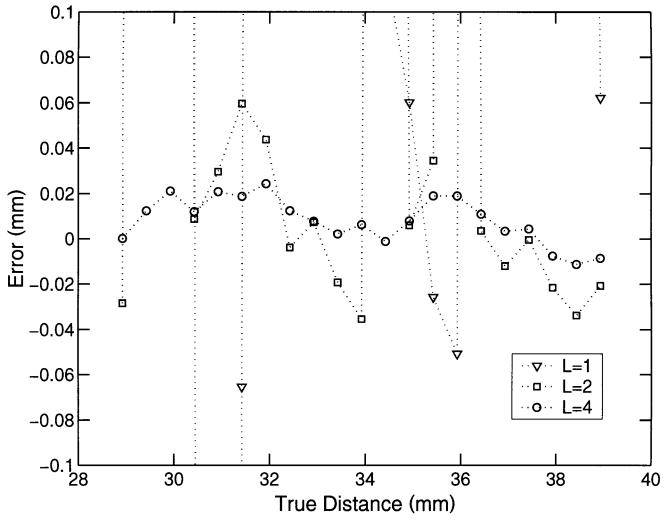

(b)

Fig. 7. Stationary level measurement results obtained by applying the multi-PEARS algorithm to the measured signal with the different choices of L. The ranging distance covers from 29 to 39 mm. The distance between two consecutive levels is 0.5 mm. (a) Measurement results versus the true distance obtained by traverse. (b) Measurement errors.

VI. Conclusion

Due to the presence of unwanted strong and closely spaced secondary echoes, it is very difficult to obtain accurate short distance measurements for acoustic proximity ranging systems using traditional matched filter based methods. In this paper, a computationally efficient time delay estimation algorithm, referred to as multi-PEARS, is presented for the joint proximity ranging and secondary echo mitigation. Numerical results demonstrate that multi-PEARS can deal with secondary echoes effectively, and the estimates obtained by using multi-PEARS can approach the corresponding CRBs as the SNR increases. Experimental results obtained by using Panasonic ceramic transducers show that multi-PEARS can also perform very well in a practical environment.

Appendix A

Derivation of PEARS

Based on the same notation for (25), the NLS cost function for the single echo case is

$$\mathcal{L}_2\left(\{\beta_1,\tau\}\right)=\left\|\mathbf{x}_1-\beta_1\mathbf{W}\mathbf{b}(\tau)\right\|^2 \tag{29}$$

where $\|\cdot\|$ denotes the Euclidean norm. Note that β_1 is nonnegative. Hence the cost function $\mathcal{L}_2$ in (29) can be expressed as

$$\begin{aligned}\mathcal{L}_2&=\left[\mathbf{x}_1-\beta_1\mathbf{W}\mathbf{b}(\tau)\right]^H\left[\mathbf{x}_1-\beta_1\mathbf{W}\mathbf{b}(\tau)\right]\\&=\mathbf{x}_1^H\mathbf{x}_1-\beta_1\mathbf{x}_1^H\mathbf{W}\mathbf{b}(\tau)-\beta_1\mathbf{b}^H(\tau)\mathbf{W}^H\mathbf{x}_1\\&\quad+\beta_1^2\mathbf{b}^H(\tau)\mathbf{W}^H\mathbf{W}\mathbf{b}(\tau)\\&=\mathbf{x}_1^H\mathbf{x}_1+\beta_1^2\mathbf{b}^H(\tau)\mathbf{W}^H\mathbf{W}\mathbf{b}(\tau)\\&\quad-2\beta_1\mathrm{Re}\left[\mathbf{b}^H(\tau)\mathbf{W}^H\mathbf{x}_1\right]\end{aligned} \tag{30}$$

where $\mathrm{Re}(x)$ is the real part of x. Since $\mathbf{x}_1^H\mathbf{x}_1+\beta_1^2\mathbf{b}^H(\tau)\mathbf{W}^H\mathbf{W}\mathbf{b}(\tau)$ is a constant and β_1 is nonnegative, the τ that minimizes $\mathcal{L}_2$ is the one that maximizes the term $2\beta_1\mathrm{Re}[\mathbf{b}^H(\tau)\mathbf{W}^H\mathbf{x}_1]$, which has the form

$$\hat{\tau}_{c_1}=\arg\max_{\tau}c_1(\tau)=\arg\max_{\tau}\mathrm{Re}\left[\mathbf{b}^H(\tau)\mathbf{W}^H\mathbf{x}_1\right]. \tag{31}$$

Note that the cost function $c_1(\tau)$ can be expressed as

$$\begin{aligned}c_1(\tau)&=\mathrm{Re}\left[\mathbf{b}^H(\tau)\mathbf{W}^H\mathbf{x}_1\right]\\&=\sum_{k=0}^{K-1}|\breve{x}_k|\cos(2\pi f_k\tau-\breve{\theta}_k)\end{aligned} \tag{32}$$

where

$$\breve{x}_k\triangleq W^*(k)x_1(k),\quad k=0,1,\ldots,K-1 \tag{33}$$

and

$$\breve{\theta}_k\triangleq-\arg(\breve{x}_k),\quad k=0,1,\ldots,K-1 \tag{34}$$

with $\arg(x)$ being the phase of x. In the absence of noise,

$$\breve{\theta}_k=2\pi f_k\tau-2\pi z_k,\quad k=0,1,\ldots,K-1 \tag{35}$$

with $\{z_k\}_{k=0}^{K-1}$ being some integers. It can be seen from (32) that $c_1(\tau)$ is a sum of K cosine functions of τ with frequencies f_0 to f_{K-1}, and hence is highly oscillatory, which makes it very difficult to find the global maximum directly.

If β_1 were complex-valued, it can be shown that minimizing $\mathcal{L}_2$ with respect to τ would yield

$$\hat{\tau}_{c_2}=\arg\max_{\tau}c_2(\tau)=\arg\max_{\tau}\left|\mathbf{b}^H(\tau)\mathbf{W}^H\mathbf{x}_1\right|. \tag{36}$$

Since $c_2(\tau)$ is much smoother than the true cost function $c_1(\tau)$, we can obtain an initial estimate based on $c_2(\tau)$ and then refine it based on $c_1(\tau)$. The first stage of PEARS is to determine an initial estimate based on $c_2(\tau)$. Note that $c_2(\tau)$ can be efficiently maximized by applying FFT with zero-padding to $\mathbf{W}^H\mathbf{x}_1$. Once the initial estimate, say $\hat{\tau}_0$, is available, we can refine it based on the true cost function $c_1(\tau)$.

Differentiating $c_1(\tau)$ with respect to τ yields

$$c_1'(\tau) = -\sum_{k=0}^{K-1} |\breve{x}_k| 2\pi f_k \sin(2\pi f_k \tau - \breve{\theta}_k). \tag{37}$$

The goal here is to approximate (37) around $\hat{\tau}_0$ with the first-order approximation to find an approximate solution to $c_1'(\tau) = 0$, which corresponds to the local maximum of $c_1(\tau)$ around $\hat{\tau}_0$. From (35), we have the following approximations at the high SNR:

$$2\pi f_k \hat{\tau}_0 \approx 2\pi z_k + \breve{\theta}_k, \quad k = 0, 1, \ldots, K-1 \tag{38}$$

where

$$z_k = \left\lfloor \frac{2\pi f_k \hat{\tau}_0 - \breve{\theta}_k}{2\pi} \right\rfloor, \quad k = 0, 1, \ldots, K-1 \tag{39}$$

with $\lfloor \cdot \rfloor$ denoting rounding to the nearest integer. In a small range around $\hat{\tau}_0$, using (38) yields the following approximations:

$$\begin{aligned} \sin(2\pi f_k \tau - \breve{\theta}_k) &= \sin(2\pi f_k \tau - \breve{\theta}_k - 2\pi z_k) \\ &\approx \sin\left[2\pi f_k (\tau - \hat{\tau}_0)\right] \\ &\approx 2\pi f_k \tau - \breve{\theta}_k - 2\pi z_k. \end{aligned} \tag{40}$$

Therefore, $c_1'(\tau)$ around $\hat{\tau}_0$ can be approximately expressed as

$$c_1'(\tau) \approx -\sum_{k=0}^{K-1} 2\pi |\breve{x}_k| f_k (2\pi f_k \tau - \breve{\theta}_k - 2\pi z_k). \tag{41}$$

Simplifying (41) and setting it to zero, we obtain the refined solution of τ as

$$\hat{\tau} = \frac{\sum_{k=0}^{K-1} |\breve{x}_k| f_k (\breve{\theta}_k + 2\pi z_k)}{\sum_{k=0}^{K-1} 2\pi |\breve{x}_k| f_k^2}. \tag{42}$$

This estimator can be interpreted as a weighted sum of K estimates of τ obtained from frequencies f_0 to f_{K-1} separately.

APPENDIX B

DERIVATION OF THE CRBS

We sketch below the derivation of the CRBs for the data model in (3) where $\{\alpha_l\}_{l=1}^{L}$ are assumed to be real-valued. Due to the conjugate symmetry property of DFTs, $\{Y(m)\}_{m=-(N/2)}^{N/2-1}$ can be expressed in terms of $\{Y(m)\}_{m=-(N/2)}^{0}$ with $\{Y(m)\}_{m=-(N/2)+1}^{-1}$ being complex-valued and $\{Y(-(N/2)), Y(0)\}$ being real-valued. Let

$$\mathbf{Y}_c = \left[Y\left(-\frac{N}{2}+1\right) \quad Y\left(-\frac{N}{2}+2\right) \quad \cdots \quad Y(-1) \right]^T \tag{43}$$

$$\mathbf{Y}_r = \left[Y\left(-\frac{N}{2}\right) \quad Y(0) \right]^T \tag{44}$$

$$\mathbf{E}_c = \left[E\left(-\frac{N}{2}+1\right) \quad E\left(-\frac{N}{2}+2\right) \quad \cdots \quad E(-1) \right]^T \tag{45}$$

$$\mathbf{E}_r = \left[E\left(-\frac{N}{2}\right) \quad E(0) \right]^T \tag{46}$$

$$\mathbf{S}_c = \left[S\left(-\frac{N}{2}+1\right) \quad S\left(-\frac{N}{2}+2\right) \quad \cdots \quad S(-1) \right]^T \tag{47}$$

$$\mathbf{S}_r = \left[S\left(-\frac{N}{2}\right) \quad S(0) \right]^T \tag{48}$$

$$\mathbf{g}(l\tau + \Delta_l) = \left[e^{-j\frac{2\pi}{NT_s}(l\tau+\Delta_l)\left(-\frac{N}{2}\right)} \quad e^{-j\frac{2\pi}{NT_s}(l\tau+\Delta_l)\left(-\frac{N}{2}+1\right)} \quad \cdots \quad 1 \right]^T \tag{49}$$

$$\mathbf{g}_c(l\tau + \Delta_l) = \left[e^{-j\frac{2\pi}{NT_s}(l\tau+\Delta_l)\left(-\frac{N}{2}+1\right)} \quad e^{-j\frac{2\pi}{NT_s}(l\tau+\Delta_l)\left(-\frac{N}{2}+2\right)} \quad \cdots \quad e^{-j\frac{2\pi}{NT_s}(l\tau+\Delta_l)(-1)} \right]^T \tag{50}$$

$$\mathbf{g}_r(l\tau + \Delta_l) = \left[e^{-j\frac{2\pi}{NT_s}(l\tau+\Delta_l)\left(-\frac{N}{2}\right)} \quad 1 \right]^T \tag{51}$$

$$\mathbf{G} = [\mathbf{g}(\tau) \quad \mathbf{g}(2\tau + \Delta_2) \quad \cdots \quad \mathbf{g}(L\tau + \Delta_L)] \tag{52}$$

$$\mathbf{G}_c = [\mathbf{g}_c(\tau) \quad \mathbf{g}_c(2\tau + \Delta_2) \quad \cdots \quad \mathbf{g}_c(L\tau + \Delta_L)] \tag{53}$$

and

$$\mathbf{G}_r = [\mathbf{g}_r(\tau) \quad \mathbf{g}_r(2\tau + \Delta_2) \quad \cdots \quad \mathbf{g}_r(L\tau + \Delta_L)]. \tag{54}$$

We have

$$\mathbf{Y}_c = \boldsymbol{\mu}_c + \mathbf{E}_c \tag{55}$$

and

$$\mathbf{Y}_r = \boldsymbol{\mu}_r + \mathbf{E}_r \tag{56}$$

where

$$\boldsymbol{\mu}_c = \mathbf{S}_c \mathbf{G}_c \boldsymbol{\alpha} \tag{57}$$

and

$$\boldsymbol{\mu}_r = \mathbf{S}_r \mathbf{G}_r \boldsymbol{\alpha} \tag{58}$$

with

$$\boldsymbol{\alpha} = [\alpha_1 \quad \alpha_2 \quad \cdots \quad \alpha_L]^T. \tag{59}$$

Assume that the additive noise $\{e(nT_S)\}_{n=0}^{N-1}$ is a real-valued zero-mean white Gaussian random process with variance σ^2. Denote

$$\boldsymbol{\theta} = [\alpha_1 \quad \cdots \quad \alpha_L \quad \tau \quad \Delta_2 \quad \cdots \quad \Delta_L \quad \sigma^2]^T. \tag{60}$$

Since the DFT matrix is a unitary operator, the joint probability density function for $\{\mathbf{Y}_c, \mathbf{Y}_r\}$ has the form

$$p(\{\mathbf{Y}_c, \mathbf{Y}_r\}|\boldsymbol{\theta}) = \frac{1}{(2\pi)^{\frac{N}{2}}\sigma^N} \exp\left\{ -\frac{1}{\sigma^2}(\mathbf{Y}_c - \boldsymbol{\mu}_c)^H (\mathbf{Y}_c - \boldsymbol{\mu}_c) - \frac{1}{2\sigma^2}(\mathbf{Y}_r - \boldsymbol{\mu}_r)^T (\mathbf{Y}_r - \boldsymbol{\mu}_r) \right\}. \tag{61}$$

Based on the extended Slepian–Bang's formula, the CRB matrix can be computed as

$$\left[\mathrm{CRB}^{-1}(\boldsymbol{\theta})\right]_{ij} = \frac{1}{2}\mathrm{tr}\left[\mathbf{Q}_r^{-1}\mathbf{Q}_{ri}'\mathbf{Q}_r^{-1}\mathbf{Q}_{rj}'\right] + \left[\boldsymbol{\mu}_{ri}'^{T}\mathbf{Q}_r{}^{-1}\boldsymbol{\mu}_{rj}'\right] \times \mathrm{tr}\left[\mathbf{Q}_c^{-1}\mathbf{Q}_{ci}'\mathbf{Q}_c^{-1}\mathbf{Q}_{cj}'\right] + 2\,\mathrm{Re}\left[\boldsymbol{\mu}_{ci}'^{H}\mathbf{Q}_c{}^{-1}\boldsymbol{\mu}_{cj}'\right] \quad (62)$$

where $\mathbf{Q}_r = \sigma^2\mathbf{I}_r$ with $\mathbf{I}_r$ being the 2×2 identity matrix, $\mathbf{Q}_c = \sigma^2\mathbf{I}_c$ with $\mathbf{I}_c$ being the $(N/2-1)\times(N/2-1)$ identity matrix, and $\mathbf{X}_i'$ denotes the derivative of $\mathbf{X}$ with respect to the ith unknown parameter. Since $\mathbf{Q}_r$ and $\mathbf{Q}_c$ do not depend on the parameters in $\boldsymbol{\mu}_r$ and $\boldsymbol{\mu}_c$, and $\boldsymbol{\mu}_r$ and $\boldsymbol{\mu}_c$ do not depend on the elements in $\mathbf{Q}_r$ and $\mathbf{Q}_c$, it can be shown that the matrix CRB($\boldsymbol{\theta}$) is block diagonal with its last row and last column being zero except for the last diagonal element. Let the signal parameter vector $\boldsymbol{\eta}$ be denoted as

$$\boldsymbol{\eta} = [\alpha_1 \quad \cdots \quad \alpha_L \quad \tau \quad \Delta_2 \quad \cdots \quad \Delta_L]^T. \quad (63)$$

Let

$$\boldsymbol{\mu} = \mathbf{W}\mathbf{G}\boldsymbol{\alpha} \quad (64)$$

with $\mathbf{W}$ being defined in (7), and $\mathbf{Q} = \sigma^2\mathbf{I}$ with $\mathbf{I}$ being the identity matrix of dimension $N/2+1$. Then

$$\left[\mathrm{CRB}^{-1}(\boldsymbol{\eta})\right]_{ij} = \left[\boldsymbol{\mu}_{ri}'^{T}\mathbf{Q}_r{}^{-1}\boldsymbol{\mu}_{rj}'\right] + 2\,\mathrm{Re}\left[\boldsymbol{\mu}_{ci}'^{H}\mathbf{Q}_c{}^{-1}\boldsymbol{\mu}_{cj}'\right] = 2\,\mathrm{Re}\left[\boldsymbol{\mu}_i'^{H}\mathbf{Q}^{-1}\boldsymbol{\mu}_j'\right]. \quad (65)$$

Define

$$\frac{\partial\boldsymbol{\mu}}{\partial\alpha_l} = \mathbf{W}\mathbf{g}(l\tau+\Delta_l), \quad l = 1,2,\ldots,L \quad (66)$$

$$\frac{\partial\boldsymbol{\mu}}{\partial\tau} = \mathbf{W}\frac{\partial\mathbf{G}}{\partial\tau}\boldsymbol{\alpha} \quad (67)$$

where

$$\frac{\partial\mathbf{G}}{\partial\tau} = \left[\frac{\partial\mathbf{g}(\tau)}{\partial\tau} \quad \frac{\partial\mathbf{g}(2\tau+\Delta_2)}{\partial\tau} \quad \cdots \quad \frac{\partial\mathbf{g}(L\tau+\Delta_L)}{\partial\tau}\right] \quad (68)$$

with

$$\frac{\partial\mathbf{g}(l\tau+\Delta_l)}{\partial\tau} = -j\frac{2\pi l}{NT_s} \times \left[\left(-\frac{N}{2}\right)e^{-j\frac{2\pi}{NT_s}(l\tau+\Delta_l)\left(-\frac{N}{2}\right)} \left(-\frac{N}{2}+1\right)e^{-j\frac{2\pi}{NT_s}(l\tau+\Delta_l)\left(-\frac{N}{2}+1\right)} \cdots \quad 0\right]^T \quad (69)$$

and

$$\frac{\partial\boldsymbol{\mu}}{\partial\Delta_l} = \mathbf{W}\frac{\partial\mathbf{g}(l\tau+\Delta_l)}{\partial\Delta_l}\alpha_l, \quad l = 2,3,\ldots,L \quad (70)$$

where

$$\frac{\partial\mathbf{g}(l\tau+\Delta_l)}{\partial\Delta_l} = -j\frac{2\pi}{NT_s}\left[\left(-\frac{N}{2}\right)e^{-j\frac{2\pi}{NT_s}(l\tau+\Delta_l)\left(-\frac{N}{2}\right)} \left(-\frac{N}{2}+1\right)e^{-j\frac{2\pi}{NT_s}(l\tau+\Delta_l)\left(-\frac{N}{2}+1\right)} \cdots \quad 0\right]^T \quad (71)$$

and

$$\mathbf{F} = \left[\frac{\partial\boldsymbol{\mu}}{\partial\alpha_1} \quad \cdots \quad \frac{\partial\boldsymbol{\mu}}{\partial\alpha_L} \quad \frac{\partial\boldsymbol{\mu}}{\partial\tau} \quad \frac{\partial\boldsymbol{\mu}}{\partial\Delta_2} \quad \cdots \quad \frac{\partial\boldsymbol{\mu}}{\partial\Delta_L}\right]. \quad (72)$$

Then

$$\mathrm{CRB}(\boldsymbol{\eta}) = \frac{\sigma^2}{2}\left[\mathrm{Re}(\mathbf{F}^H\mathbf{F})\right]^{-1} \quad (73)$$

which is easily evaluated numerically.

REFERENCES

[1] W. Göpel, J. Hesse, and J. N. Zemel, *Sensors: A Comprehensive Survey*. Weinheim, Germany: Wiley-VCH, 1989.

[2] O. Brand and H. Baltes, "Micromachined resonant sensors: an overview," in *Sensors Update*, H. Baltes, W. Göpel, and J. Hesse, Eds. Weinheim, Germany: Wiley-VCH, 1998, vol. 4, pp. 3–51.

[3] W. Manthey, N. Kroemer, and V. Mágori, "Ultrasonic transducers and transducer arrays for applications in air," *Meas. Sci. Technol.*, vol. 3, pp. 249–261, 1992.

[4] S. Ashley, "Wrap drive underwater," *Sci. Amer.*, vol. 284, pp. 70–79, May 2001.

[5] D. P. Massa, "Choosing an ultrasonic sensor for proximity or distance measurement. Part 1," *Sensors*, vol. 16, pp. 34–37, Feb. 1999.

[6] Massa Products Corporation. [Online] http://www.massa.com.

[7] Migatron, Inc. [Online] http://www.migatron.com.

[8] R. Wu and J. Li, "An efficient algorithm for time delay estimation," *IEEE Trans. Signal Processing*, vol. 46, pp. 2231–2235, Aug. 1998.

[9] J. E. Ehrenberg, T. E. Ewart, and R. D. Morris, "Signal-processing techniques for resolving individual pulses in a multipath signal," *J. Acoust. Soc. Amer.*, vol. 63, pp. 1861–1865, June 1978.

[10] R. Wu and J. Li, "Time-delay estimation via optimizing highly oscillatory cost functions," *IEEE J. Ocean. Eng.*, vol. 23, pp. 235–244, July 1998.

[11] R. Wu, J. Li, and Z. Liu, "Super resolution time delay estimation via MODE-WRELAX," *IEEE Trans. Aerosp. Electron. Syst.*, vol. 35, pp. 294–307, Jan. 1999.

[12] J. Li and P. Stoica, "Efficient mixed-spectrum estimation with applications to target feature extraction," *IEEE Trans. Signal Processing*, vol. 44, pp. 281–295, Feb. 1996.

[13] H. Li, P. Stoica, and J. Li, "Computationally efficient parameter estimation for harmonic sinusoidal signals," *Signal Processing*, vol. 80, pp. 1937–1944, 2000.

[14] B. G. Quinn and P. J. Thomson, "Estimating the frequency of a periodic function," *Biometrika*, vol. 78, pp. 65–74, Mar. 1991.

[15] M. Zeytinoğlu and K. M. Wong, "Detection of harmonic sets," *IEEE Trans. Signal Processing*, vol. 43, pp. 2618–2630, Nov. 1995.

[16] X. Li, R. Wu, S. Rasmi, J. Li, L. N. Cattafesta, and M. Sheplak, "An acoustic proximity ranging system for monitoring the cavity thickness," *IEEE Trans. Ultrason., Ferroelect., Freq. Contr.*, vol. 50, pp. 898–910, July 2003.

[17] P. Stoica and R. L. Moses, *Introduction to Spectral Analysis*. Upper Saddle River, NJ: Prentice–Hall, 1997.

[18] T. Söderström and P. Stoica, *System Identification*. London, U.K.: Prentice-Hall International, 1989.

[19] X. Li, R. Wu, M. Sheplak, and J. Li, "Multifrequency CW-based time-delay estimation for proximity ultrasonic sensors," *Proc. IEEE Radar, Sonar and Navigation*, vol. 149, pp. 53–59, Apr. 2002.

[20] Panasonic Corp., Ultrasonic Ceramic Sensors, Burlington, MA, 2001.

[21] J. D. Anderson, *Modern Compressible Flow*. New York: McGraw-Hill, 1990.

[22] J. Jacob Fraden, *Handbook of Modern Sensors*, 2nd ed. Woodbury, New York: Amer. Inst. Phys., 1997, ch. 5, pp. 233–278.

Xi Li (S'0l) received the B.Sc and Ph.D. degrees in electrical engineering from Nanjing University of Science and Technology (NUST), Nanjing, China, in 1995 and 1999, respectively. He is currently pursuing the Ph.D. degree in electrical engineering, with a minor in aerospace engineering, at the University of Florida, Gainesville.

Since May 2000, he has been a Research Assistant in the Department of Electrical and Computer Engineering at the University of Florida. His research interests include spectral estimation and signal processing for acoustic and radar applications.

Renbiao Wu (M'95–SM'01) received the B.Sc. and M.Sc. degrees in electrical engineering from Northwestern Polytechnic University, Xian, China, in 1988 and 1991, respectively, and the Ph.D. degree in electrical engineering from Xidian University, Xian, in 1994.

From May 1994 to February 1996, he was a Postdoctoral Fellow at the College of Marine Engineering, Northwestern Polytechnic University, where he was promoted to Associate Professor in December 1995. From March 1996 to February 1997, he was a Visiting Scholar at the Center for Transportation Research, Virginia Polytechnic Institute and State University, Blacksburg. From March 1997 to December 1998, he was a Visiting Scholar in the Department of Electrical and Computer Engineering, University of Florida, Gainesville. Since January 1999, he has been with the Department of Communications Engineering, College of Air Traffic Management, Civil Aviation University of China, Tianjin, China, where he is currently a Chaired Professor of Tianjin. His research interests include spectral estimation, feature extraction and image formation, space-time adaptive processing, and adaptive arrays and their applications to radar and wireless communications systems.

Srihari Rasmi received the B.Tech. degree in naval architecture from the Indian Institute of Technology, Madras, India in 1999. He is currently pursuing the M.S degree in the areas of experimental fluid dynamics and signal processing at the Department of Mechanical and Aerospace Engineering at the University of Florida, Gainesville.

From December 1998 to April 1999, he received a scholarship to pursue his research interests related to stability of ships at Hochshule Bremen in Bremen, Germany. From August to December of 1999, he was an Academic Visitor at the Ship Stability Research Centre, University of Strathclyde, Glasgow, U.K.

Jian Li (S'87–M'91–SM'97) received the M.Sc. and Ph.D. degrees in electrical engineering from The Ohio State University, Columbus, in 1987 and 1991, respectively.

From April 1991 to June 1991, she was an Adjunct Assistant Professor with the Department of Electrical Engineering, The Ohio State University. From July 1991 to June 1993, she was an Assistant Professor with the Department of Electrical Engineering, University of Kentucky, Lexington. Since August 1993, she has been with the Department of Electrical and Computer Engineering, University of Florida, Gainesville, where she is currently a Professor. Her current research interests include spectral estimation, array signal processing, and signal processing for wireless communications and radar. She is currently a Guest Editor for *Multidimensional Systems and Signal Processing*.

Dr. Li is a member of Sigma Xi and Phi Kappa Phi. She received the 1994 National Science Foundation Young Investigator Award and the 1996 Office of Naval Research Young Investigator Award. She is currently an Associate Editor for the IEEE TRANSACTIONS ON SIGNAL PROCESSING.

Louis N. Cattafesta, III, received the B.S. degree in mechanical engineering with Highest Distinction from the Pennsylvania State University, University Park, in 1986, the M.S. degree in Aeronautics from the Massachusetts Institute of Technology, Cambridge, in 1988, and the Ph.D. degree in mechanical engineering from the Pennsylvania State University in 1992.

He is currently an Associate Professor with the Department of Mechanical and Aerospace Engineering, University of Florida (UF), Gainesville. Prior to joining UF in April of 1999, he was a Senior Research Scientist at High Technology Corporation, Hampton, VA, where he was the Group Leader of the Experimental and Instrumentation Group. In 1992, he joined High Technology Corporation as a Research Scientist at NASA Langley Research Center. His research at NASA Langley focused on supersonic laminar flow control and pressure- and temperature-sensitive paint measurement techniques. He subsequently became involved in active control of flow-induced cavity oscillations. His current research interests lie in active flow and noise control, particularly the modeling and design of piezoelectric actuators and MEMS sensors and also the development and implementation of real-time, adaptive flow control schemes.

Dr. Cattafesta is a member of the AIAA Aerodynamic Measurement Technology Technical Committee.

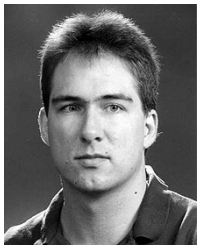

Mark Sheplak received the B.S., M.S., and Ph.D. degrees in mechanical engineering from Syracuse University, Syracuse, NY, in 1989, 1992, and 1995, respectively.

He is currently an Associate Professor with the Department of Mechanical and Aerospace Engineering, University of Florida (UF). Prior to joining UF in 1998, he was a Postdoctoral Associate at the Massachusetts Institute of Technology's Microsystems Technology Laboratories, Cambridge, from 1995 to 1998. During his Ph.D. studies he was a GSRP Fellow at NASA-LaRC, Hampton, VA, from 1992 to 1995. His current research focuses on the design, fabrication, and characterization of high-performance, instrumentation-grade, MEMS-based sensors and actuators that enable the measurement, modeling, and control of various physical properties.